Commun. Comput. Phys.
doi: 10.4208/cicp.OA-2018-0325

Vol. **27**, No. 2, pp. 480-502
February 2020

Finite-Volume-Particle Methods for the Two-Component Camassa-Holm System

Alina Chertock[1], Alexander Kurganov[2,3] and Yongle Liu[2,4,*]

[1] *Department of Mathematics, North Carolina State University, Raleigh, NC 27695, USA.*
[2] *Department of Mathematics, Southern University of Science and Technology, Shenzhen, 518055, China.*
[3] *SUSTech International Center for Mathematics, Southern University of Science and Technology, Shenzhen, 518055, China.*
[4] *Department of Mathematics, Harbin Institute of Technology, Haerbin, 150001, China.*

Received 27 December 2018; Accepted (in revised version) 25 March 2019

Abstract. We study the two-component Camassa-Holm (2CH) equations as a model for the long time water wave propagation. Compared with the classical Saint-Venant system, it has the advantage of preserving the waves amplitude and shape for a long time. We present two different numerical methods—finite volume (FV) and hybrid finite-volume-particle (FVP) ones. In the FV setup, we rewrite the 2CH equations in a conservative form and numerically solve it by the central-upwind scheme, while in the FVP method, we apply the central-upwind scheme to the density equation only while solving the momentum and velocity equations by a deterministic particle method. Numerical examples are shown to verify the accuracy of both FV and FVP methods. The obtained results demonstrate that the FVP method outperforms the FV method and achieves a superior resolution thanks to a low-diffusive nature of a particle approximation.

AMS subject classifications: 65M08, 76M12, 76M28, 86-08, 76M25, 35L65

Key words: Two-component Camassa-Holm system, finite-volume method, deterministic particle method, finite-volume-particle method, central-upwind scheme.

1 Introduction

Due to the potential tragic nature of tsunami waves, there is a need for the scientific understanding and modeling of this complicated phenomenon in order to reduce unwanted destruction and prevent unnecessary deaths from this natural disaster. Tsunami

*Corresponding author. *Email addresses:* chertock@math.ncsu.edu (A. Chertock), alexander@sustech.edu.cn (A. Kurganov), 11749318@mail.sustech.edu.cn (Y.-L. Liu)

waves are caused by the displacement of a large volume of a body of water, typically an ocean or a large lake; see, e.g., [6, 48, 49]. They do not resemble other sea waves and are instead characterized by having relatively low amplitude (wave height) offshore, large wavelength, and large characteristic wave speed. This characterization is what prevents tsunami waves from being felt at sea. Tsunami waves grow in height as they reach shallowing water, in what is known as a *wave shoaling* process. In this process, the wave slows down, the wavelength decreases, and a very high and powerful wave arrives on the shore and may cause massive destruction.

There have been many attempts to create accurate models and corresponding numerical methods for simulating tsunami waves. One popular model in the shallow water wave theory is the classical Saint-Venant (SV) system [27], which approximates the behavior of real ocean waves in a reasonable way and is a depth-averaged system that can be derived from the Navier-Stokes equations; see, e.g., [35, 43, 50]. The SV system is widely used to describe flows in lakes, rivers and coastal areas, in which the typical time and space scales of interest are relatively short. Since the SV system is quite difficult to solve, it is sometimes simplified in a number of ways, including linearization, in which the velocity of water particles is taken to be the gradient of a scalar potential. Taking various asymptotic limits of the inviscid Euler equations results in a host of integrable and nearly integrable equations such as the Korteweg-de Vries (KdV) equation, Camassa-Holm (CH) equation, nonlinear Schrödinger equation, and so on; see, e.g., [7, 36, 53, 56]. Unfortunately, while these equations have exact (integrable) solutions, they also diverge from the true behavior described by the full equations for any but very short time scales.

Tsunami waves form in deep water and travel very long distances (thousands of kilometers) before coming to shore. Over long time, solutions of the SV system break down, dissipate in an unphysical manner, develop shock waves, and fails to capture small, trailing waves that are seen in nature and laboratory experiments. Thus, it is necessary to use a more sophisticated model in order to preserve the wave characteristics over long time simulations.

Non-hydrostatic models (the celebrated Green-Naghdi (GN) equations [31] and several others; see, e.g., [1–3] and references therein) work well for long-time propagation of tsunami-type waves because they allow the wave to travel for long distances without changing the shape or decaying in amplitude. In addition, since these systems are dispersive, they give rise to trailing waves that are observed to follow tsunamis in nature. It is, however, necessary to achieve some balance between dispersion observed with a non-hydrostatic model and dissipation seen in the classical SV system.

One attempt to achieve such a balance was made in [4, 5], where the non-hydrostatic SV system was rigorously derived from the GN equations. As it has been demonstrated in [16], the non-hydrostatic SV system is capable of accurately modeling long-time propagation of tsunami-type waves. However, the system is quite complicated and developing accurate, robust and efficient numerical methods for computing its solutions is a highly nontrivial task.

Another system that has been derived from the GN equations is a two-component

generalization of the CH equation, for which the integrability property associated with the CH equation has been combined with compressibility; see, e.g., [24, 32, 52]. Compared with the original CH equation, the two-component Camassa-Holm (2CH) system contains an additional continuity equation for the scalar density ρ, and the momentum (velocity) equation contains a pressure term involving density:

$$\rho_t+(\rho u)_x=0, \tag{1.1a}$$

$$m_t+um_x+2mu_x=-\frac{g}{2}(\rho^2)_x. \tag{1.1b}$$

Here, $m(x,t)$ is the momentum related to the fluid velocity $u(x,t)$ through the modified Helmholtz equation,

$$m=u-\alpha^2u_{xx}, \tag{1.1c}$$

the density $\rho(x,t)$ is related to the total depth of the water column (see Section 3.2), $\alpha>0$ is a length scale, and $g>0$ is the constant gravitational acceleration.

This paper focuses on the development of numerical methods for the 2CH system. Several methods have been already developed and are available in the literature. In [23], a multi-symplectic structure of the 2CH system was established and then used to derive a multi-symplectic numerical method. Invariant-preserving finite-difference schemes for both the CH equation and 2CH system were introduced in [46]. Very recently a new fifth-order spatially accurate upwinding combined compact difference (UCCD5) scheme for the 2CH system has been presented in [57]. The main idea of this method is to solve the 2CH system in three steps: first, to solve the time-dependent equation for the horizontal fluid velocity with nonlinear convection, then an inhomogeneous Helmholtz equation, and finally the density transport equation.

In this paper, we develop two alternative numerical methods for the 2CH system and numerically demonstrate that the 2CH system may serve as a viable model for the long time propagation of tsunami-type waves. First, we derive a finite-volume central-upwind scheme for the system (1.1). Central-upwind schemes have been originally developed for hyperbolic systems of conservation laws [38, 40, 42] and then extended and applied to hyperbolic systems of balance laws arising in modeling shallow water flows; see, e.g., [10, 11, 16, 37, 39, 41]. In order to apply the central-upwind scheme to the system (1.1), we rewrite Eqs. (1.1a) and (1.1b) in the following conservative form:

$$\begin{aligned}&\rho_t+(\rho u)_x=0,\\&m_t+\left(um+\frac{1}{2}u^2-\frac{\alpha^2}{2}u_x^2+\frac{1}{2}g\rho^2\right)_x=0,\end{aligned} \tag{1.2}$$

and then implement the central-upwind scheme for the system (1.2) in quite a straightforward manner as described in Section 2.1.

Even though the designed finite-volume (FV) method is robust and efficient, it suffers from an excessive numerical dissipation the same way the central-upwind scheme

for the original CH equation did; see [22]. To reduce the amount of the numerical diffusion, we follow the idea presented in [13, 14, 17] and derive a hybrid finite-volume-particle (FVP) method for the system (1.1). In the hybrid approach, the density equation (1.1a) is solved using the finite-volume central-upwind scheme, while the momentum and velocity equations (1.1b) and (1.1c) are solved by a deterministic particle method. Particle methods were originally introduced for solving linear transport equations (see, e.g., [26, 51]), but in recent years have also been used for approximating solutions of a variety of time-dependent PDEs, see, e.g., [15, 19, 20, 28, 45]. In particular, the particle method has been successfully applied to the original CH equation in [8, 9, 12, 21, 22].

Finally, we perform several numerical experiments to study the effect of the dispersive parameter α in (1.1c) and to compare the performance of the central-upwind scheme and hybrid FVP method. The obtained results demonstrate that for certain choices of α the amplitude and speed of the wave is preserved for much longer times than in the non-dispersive case of $\alpha=0$.

2 Numerical methods for the 2CH system

In this section, we describe the two numerical methods which will be pertinent to our study of modeling the propagation of tsunami waves.

2.1 Central-upwind scheme

We start by describing a semi-discrete second-order central-upwind scheme applied to the system (1.2), (1.1c). We first rewrite (1.2) in the vector form as

$$\boldsymbol{q}_t+\boldsymbol{f}(\boldsymbol{q})_x=\boldsymbol{0},$$

with

$$\boldsymbol{q}=\begin{pmatrix}\rho\\ m\end{pmatrix},\qquad \boldsymbol{f}(\boldsymbol{q})=\begin{pmatrix}\rho u\\ mu+\dfrac{1}{2}u^2-\dfrac{\alpha^2}{2}u_x^2+\dfrac{g}{2}\rho^2\end{pmatrix}, \tag{2.1}$$

where u globally depends on m through the modified Helmholtz equation (1.1c).

We divide the computational domain Ω into the cells $C_j:=[x_{j-\frac{1}{2}},x_{j+\frac{1}{2}}]$, which are, for simplicity, assumed to be uniform, that is, $x_{j+\frac{1}{2}}-x_{j-\frac{1}{2}}\equiv\Delta x$. We denote by $\overline{\boldsymbol{q}}_j(t):\approx\frac{1}{\Delta x}\int_{C_j}\boldsymbol{q}(x,t)\,\mathrm{d}x$ the computed cell averages of $\boldsymbol{q}$, which are assumed to be available at time t and then evolved in time by solving the following system of ODEs:

$$\frac{\mathrm{d}}{\mathrm{d}t}\overline{\boldsymbol{q}}_j(t)=-\frac{\boldsymbol{\mathcal{F}}_{j+\frac{1}{2}}(t)-\boldsymbol{\mathcal{F}}_{j-\frac{1}{2}}(t)}{\Delta x}, \tag{2.2}$$

where $\boldsymbol{\mathcal{F}}_{j+\frac{1}{2}}(t)$ are numerical fluxes. We use the central-upwind fluxes from [38] (for convenience, we will omit the dependence of all of the indexed finite-volume quantities

on t in the rest of this paper):

$$\mathcal{F}_{j+\frac{1}{2}}=\frac{a^+_{j+\frac{1}{2}}f\big(q^-_{j+\frac{1}{2}}\big)-a^-_{j+\frac{1}{2}}f\big(q^+_{j+\frac{1}{2}}\big)}{a^+_{j+\frac{1}{2}}-a^-_{j+\frac{1}{2}}}+a^+_{j+\frac{1}{2}}a^-_{j+\frac{1}{2}}\left[\frac{q^+_{j+\frac{1}{2}}-q^-_{j+\frac{1}{2}}}{a^+_{j+\frac{1}{2}}-a^-_{j+\frac{1}{2}}}-d_{j+\frac{1}{2}}\right], \tag{2.3}$$

where $q^{\pm}_{j+\frac{1}{2}}$ are the right/left point values of the conservative variable q at the cell interfaces, $a^{\pm}_{j+\frac{1}{2}}$ are the right-/left-sided local speeds of propagation, and $d_{j+\frac{1}{2}}$ is a built-in "anti-diffusion" term given by

$$d_{j+\frac{1}{2}}=\text{minmod}\left(\frac{q^+_{j+\frac{1}{2}}-q^*_{j+\frac{1}{2}}}{a^+_{j+\frac{1}{2}}-a^-_{j+\frac{1}{2}}},\frac{q^*_{j+\frac{1}{2}}-q^-_{j+\frac{1}{2}}}{a^+_{j+\frac{1}{2}}-a^-_{j+\frac{1}{2}}}\right), \tag{2.4}$$

where

$$q^*_{j+\frac{1}{2}}=\frac{a^+_{j+\frac{1}{2}}q^+_{j+\frac{1}{2}}-a^-_{j+\frac{1}{2}}q^-_{j+\frac{1}{2}}-\Big\{f\big(q^+_{j+\frac{1}{2}}\big)-f\big(q^-_{j+\frac{1}{2}}\big)\Big\}}{a^+_{j+\frac{1}{2}}-a^-_{j+\frac{1}{2}}}. \tag{2.5}$$

We compute the point values $q^{\pm}_{j+\frac{1}{2}}$ in (2.3) using a second-order piecewise linear approximation,

$$\widetilde{q}(x)=\overline{q}_j+(q_x)_j(x-x_j),\quad x\in C_j, \tag{2.6}$$

where $x_j:=(x_{j-\frac{1}{2}}+x_{j+\frac{1}{2}})/2$. A non-oscillatory nature of $\widetilde{q}$ is enforced by computing the slopes $(q_x)_j$ using a nonlinear limiter. In the numerical experiments reported in §3, we have used the generalized minmod limiter (see, e.g., [44,47,54,55]):

$$(q_x)_j=\text{minmod}\left(\theta\frac{\overline{q}_j-\overline{q}_{j-1}}{\Delta x},\frac{\overline{q}_{j+1}-\overline{q}_{j-1}}{2\Delta x},\theta\frac{\overline{q}_{j+1}-\overline{q}_j}{\Delta x}\right), \tag{2.7}$$

where $\theta\in[1,2]$ is the parameter that helps to control the amount of numerical diffusion (larger values of θ correspond to less diffusive, but more oscillatory reconstruction), and the minmod function,

$$\text{minmod}(z_1,z_2,\cdots):=\begin{cases}\min\limits_j\{z_j\}, & \text{if } z_j>0\ \forall j,\\ \max\limits_j\{z_j\}, & \text{if } z_j<0\ \forall j,\\ 0, & \text{otherwise,}\end{cases}$$

is applied to the vector quantities in a component-wise manner.

Given the piecewise polynomial reconstruction (2.6), we obtain the point values of q at each cell interface:

$$q^+_{j+\frac{1}{2}}=\overline{q}_{j+1}-\frac{\Delta x}{2}(q_x)_{j+1},\qquad q^-_{j+\frac{1}{2}}=\overline{q}_j+\frac{\Delta x}{2}(q_x)_j. \tag{2.8}$$

In the non-dispersive case, that is, when $\alpha=0$ and thus $u\equiv m$, the right- and left-sided local speeds of propagation can be easily estimated using the largest and smallest eigenvalues of the Jacobian

$$\frac{\partial \boldsymbol{f}}{\partial \boldsymbol{q}}=\begin{pmatrix} m & \rho \\ g\rho & 3m \end{pmatrix}\equiv\begin{pmatrix} u & \rho \\ g\rho & 3u \end{pmatrix},$$

that is, we have

$$\begin{aligned} a^+_{j+\frac12}&=\max\left\{2u^-_{j+\frac12}+\sqrt{\left(u^-_{j+\frac12}\right)^2+g\left(\rho^-_{j+\frac12}\right)^2},2u^+_{j+\frac12}+\sqrt{\left(u^+_{j+\frac12}\right)^2+g\left(\rho^+_{j+\frac12}\right)^2},0\right\},\\ a^-_{j+\frac12}&=\min\left\{2u^-_{j+\frac12}-\sqrt{\left(u^-_{j+\frac12}\right)^2+g\left(\rho^-_{j+\frac12}\right)^2},2u^+_{j+\frac12}-\sqrt{\left(u^+_{j+\frac12}\right)^2+g\left(\rho^+_{j+\frac12}\right)^2},0\right\}. \end{aligned} \tag{2.9}$$

In the dispersive case, that is, when $\alpha\neq0$, there is a global dependence of u on m and formula (2.9) is not true any more. We still, however, use (2.9) to estimate the one-sided local speeds as the presence of dispersive terms leads to the appearance of smooth dispersive waves and smears shock waves (present in a non-dispersive case) without affecting the speed of shock-like and solitary waves, as demonstrated in the numerical examples reported in Section 3.2; see Example 4. In order to use formula (2.9), the values of the velocities at cell interfaces, $u^\pm_{j+\frac12}$, are obtained as follows. We first use the second-order finite-difference central scheme to solve the modified Helmholtz equation (1.1c) and recover the cell interface point values $\{u_{j+\frac12}\}$ from $\{m_{j+\frac12}\}$, where $m_{j+\frac12}:=\left(m^+_{j+\frac12}+m^-_{j+\frac12}\right)/2$ and the cell interface values $m^\pm_{j+\frac12}$ are computed by (2.8). Then, thanks to the continuity of u, we have cell interface values $u^\pm_{j+\frac12}=u_{j+\frac12}$.

It should be observed that one needs not only to compute the velocity point values $u^\pm_{j+\frac12}$ at cell interfaces but also its derivatives, which are required for computing the numerical fluxes, see formula (2.1) and (2.3). The latter can be done by first computing the values $(u_x)_j=(u_{j+\frac12}-u_{j-\frac12})/\Delta x$ and then using the reconstruction procedure according to formulae (2.7)-(2.8).

Finally, we remark that the resulting semi-discrete central-upwind scheme (2.2), (2.3) is a system of time dependent ODEs, which has to be solved using an appropriate ODE solver. In our numerical experiments, we have used the three-stage third-order strong stability preserving (SSP) Runge-Kutta method (see, e.g., [29,30]) with an adaptive time step computed at every time level using the CFL number 1/2:

$$\Delta t^{\rm FV}=\frac{\Delta x}{2a_{\max}},\qquad a_{\max}:=\max_j\left\{a^+_{j+\frac12},-a^-_{j+\frac12}\right\}. \tag{2.10}$$

2.2 Hybrid Finite-Volume-Particle (FVP) method

In this section, we present a hybrid FVP method, which utilizes the strengths of both finite-volume and particle methods: the continuity equation (1.1a) is numerically solved

using the central-upwind scheme described in Section 2.1, while the momentum and velocity equations, (1.1b) and (1.1c), are numerically solved by a deterministic particle method.

Let us assume that at some time level t the computed solution is available. As in §2.1, the density ρ is realized in terms its cell averages, $\{\overline{\rho}_j\}$, and the corresponding piecewise linear reconstruction

$$\widetilde{\rho}(x)=\overline{\rho}_j+(\rho_x)_j(x-x_j),\quad x\in C_j, \tag{2.11}$$

where the slopes $(\rho_x)_j$ are computed using the minmod limiter as in the first component of (2.7). On the other hand, the particle approximation of the momentum m at the time level t is given in the form of a linear combination of Dirac δ-functions,

$$m^N(x,t)=\sum_{i=1}^{N}w_i(t)\delta(x-x_i^{\rm p}(t)), \tag{2.12}$$

where $x_i^{\rm p}(t)$ and $w_i(t)$ represent the location and weight of the i-th particle, respectively, and N denotes the total number of particles in the computational domain Ω.

Using (1.1c), one can directly compute the velocity u from the particle distribution of the momentum (2.12) (see [12]): u can be obtained by taking the convolution product $u=G*m$, where

$$G(|x-y|)=\frac{1}{2\alpha}e^{-|x-y|/\alpha}$$

is the Green's function associated with the Helmholtz operator in (1.1c). Thus, we have the following approximation of u at the time level t:

$$u^N(x,t)=\Big(G*m^N\Big)(x,t)=\frac{1}{2\alpha}\sum_{i=1}^{N}w_i(t)e^{-|x-x_i^{\rm p}(t)|/\alpha}. \tag{2.13}$$

The solution is then evolved in time according to the following algorithm. First, the cell averages $\{\overline{\rho}_j\}$ are evolved using the semi-discrete central-upwind scheme described in §2.1:

$$\frac{\rm d}{{\rm d}t}\overline{\rho}_j=-\frac{\mathcal{F}_{j+\frac12}-\mathcal{F}_{j-\frac12}}{\Delta x}, \tag{2.14}$$

where

$$\mathcal{F}_{j+\frac12}=\frac{\Big(a^+_{j+\frac12}\rho^-_{j+\frac12}-a^-_{j+\frac12}\rho^+_{j+\frac12}\Big)u_{j+\frac12}}{a^+_{j+\frac12}-a^-_{j+\frac12}}+a^+_{j+\frac12}a^-_{j+\frac12}\left[\frac{\rho^+_{j+\frac12}-\rho^-_{j+\frac12}}{a^+_{j+\frac12}-a^-_{j+\frac12}}-d_{j+\frac12}\right].$$

Here, $\rho^\pm_{j+\frac12}$ are the right/left point values of ρ reconstructed using (2.11), $u_{j+\frac12}=u^N(x_{j+\frac12})$ is the velocity obtained from (2.13), and the one-sided local speeds $a^\pm_{j+\frac12}$ are estimated using (2.9) with $u^\pm_{j+\frac12}=u_{j+\frac12}$. The built-in "anti-diffusion" $d_{j+\frac12}$ is obtained using the first component of (2.4), (2.5).

Next, following [12,21,22], we substitute (2.12) into a weak formulation of (1.1b) and obtain the following system of ODEs for $x_i^{\rm p}$ and w_i:

$$\begin{cases} \dfrac{{\rm d}x_i^{\rm p}(t)}{{\rm d}t} = u^N(x_i^{\rm p}(t),t), \\ \dfrac{{\rm d}w_i(t)}{{\rm d}t} + u_x^N(x_i^{\rm p}(t),t)w_i(t) = \beta_i(t). \end{cases} \tag{2.15}$$

Here, $u_x(x_i^{\rm p}(t),t)$ should be computed using the velocity given by (2.13). One may follow the approach in [12,21,22] and simply differentiate (2.13), which results in

$$u_x^N(x,t) = \Big(G_x * m^N\Big)(x,t) = -\frac{1}{2\alpha^2}\sum_{j=1}^N w_j(t)\,{\rm sgn}(x-x_j^{\rm p}(t))e^{-|x-x_j^{\rm p}(t)|/\alpha}. \tag{2.16}$$

Next, we consider $\beta_i(t)$, which is the contribution associated with the term $-\frac{g}{2}(\rho^2)_x$, namely,

$$\beta_i(t) = -\int\limits_{\Omega_i(t)} \frac{g}{2}(\rho^2)_x {\rm d}x. \tag{2.17}$$

Here, $\Omega_i(t)$ is a domain that includes the i-th particle and satisfies the following properties:

$$w_i(t) = \int\limits_{\Omega_i(t)} m(x,t){\rm d}x, \quad \Omega_1(t)\oplus\cdots\oplus\Omega_N(t) = \Omega. \tag{2.18}$$

In general, $\Omega_i(t)$ is not known (see, e.g., [15]), but it can be approximated by

$$\Omega_i(t) \approx \big[x_{i-\frac12}^{\rm p}(t), x_{i+\frac12}^{\rm p}(t)\big], \quad x_{i+\frac12}^{\rm p}(t) = \frac{x_i^{\rm p}(t)+x_{i+1}^{\rm p}(t)}{2}, \tag{2.19}$$

and thus the integration in (2.17) results in

$$\beta_i(t) = -\frac{g}{2}\Big\{\rho^2\big(x_{i+\frac12}^{\rm p}(t)\big) - \rho^2\big(x_{i-\frac12}^{\rm p}(t)\big)\Big\},$$

where $\rho\big(x_{i+\frac12}^{\rm p}(t)\big) = \widetilde{\rho}\big(x_{i+\frac12}^{\rm p}(t)\big)$ are obtained using the piecewise linear reconstruction (2.11). To this end, one needs to find out which cell the point $x_{i+\frac12}^{\rm p}(t)$ is located in. This can be efficiently done since by a time step restriction associated with the particle method, every particle can either remain in the same cell or move to the neighboring cell within one time step.

The ODE system (2.14), (2.15) is to be integrated by an appropriate ODE solver. In our numerical experiments, we have used the three-stage third-order SSP Runge-Kutta method. The initial positions of particles, $x_i^{\rm p}(0)$, and their initial weights, $w_i(0)$, are chosen so that

$$m^N(x,0) = \sum_{i=1}^N w_i(0)\delta(x-x_i^{\rm p}(0))$$

represents a high-order approximation of the initial data $m(x,0)$ at time $t=0$. One way of obtaining such an approximation is to use (2.18), (2.19) at $t=0$. For example, a second-order midpoint quadrature applied to the integral in (2.18) will lead to $w_i(0)=|\Omega_i(0)|m(x_i^{\rm p}(0),0)$.

We note that the time step given by (2.10) may now need to be reduced, since we do not allow the particle trajectories to intersect in the (x,t)-plane as such an intersection is unphysical. This is achieved by imposing a more severe restriction on Δt, namely, we take

$$\Delta t^{\rm FVP}=\min(\Delta t^{\rm FV},\Delta t^*), \tag{2.20}$$

where $\Delta t^{\rm FV}$ is given by (2.10) and

$$\Delta t^*=\begin{cases}\dfrac{x_{i+1}^{\rm p}(t)-x_i^{\rm p}(t)}{u_i^{\rm p}(t)-u_{i+1}^{\rm p}(t)}, & \text{if } u_i^{\rm p}(t)>u_{i+1}^{\rm p}(t),\\ \Delta t^{\rm FV}, & \text{otherwise.}\end{cases} \tag{2.21}$$

Particle merger. We would like to point out that the proposed FVP method may suffer from one obvious drawback: If the distance between any two particles, $x_{i+1}^{\rm p}(t)-x_i^{\rm p}(t)$, becomes too small, then the time step $\Delta t^{\rm FVP}$ given by (2.20) and (2.21) may also become very small, which would make the FVP method extremely inefficient.

In order to avoid this problem, we use the same particle merger technique which was used in [18]. Namely, if at some time level $x_{i+1}^{\rm p}(t)-x_i^{\rm p}(t)$ becomes smaller than a critical threshold value, which we take to be $d_{cr}\cdot L/N_p$, where L is the length of the computational domain, N_p is the initial number of particles and $d_{cr}<1$ is a prescribed number, the i^{th} and $(i+1)^{th}$ particles are merged into a new one. The new particle is located at the center of mass of the replaced particles, that is,

$$\widehat{x}=\frac{w_i^{\rm p}(t)x_i^{\rm p}(t)+w_{i+1}^{\rm p}(t)x_{i+1}^{\rm p}(t)}{w_i^{\rm p}(t)+w_{i+1}^{\rm p}(t)},$$

its weight is

$$\widehat{w}=w_i^{\rm p}(t)+w_{i+1}^{\rm p}(t),$$

and the cell occupied by the new particle is then set to be the union of $\Omega_i(t)$ and $\Omega_{i+1}(t)$, so that

$$|\widehat{\Omega}|=|\Omega_i(t)|+|\Omega_{i+1}(t)|.$$

After the merger, the particles are renumbered and their total number is reduced by one.

3 Numerical examples

In this section, we present several numerical experiments to demonstrate the performance of the proposed finite-volume (FV) and hybrid FVP methods. In all of the ex-

periments, we take the minmod parameter $\theta=1.3$, prescribed number $d_{cr}=0.1$ and consider the periodic boundary conditions. Notice that due to the periodicity, we replace $|x-x_i^{\rm p}(t)|$ with $\min\{|x-x_i^{\rm p}(t)|,L-|x-x_i^{\rm p}(t)|\}$ in (2.13) and (2.16) as well as in (3.1) and (3.2). In all of the figures, "FV(N_x)" stands for the FV method with N_x FV cells, while "FVP(N_x,N_p,$N_{\tilde{p}}$)" stands for the FVP method with N_x FV cells, N_p initial particles and $N_{\tilde{p}}$ particles at the final time.

3.1 Accuracy tests

We first test the accuracy of studied FV and FVP methods on three numerical examples. Since the solutions in all of them are nonsmooth, we either compute the L^1-errors or verify the conservation of the discretized Hamiltonians. In these three examples, we set $\alpha=1$ and $g=1$.

Example 1 — Dam break problem

In the first example taken from [46], we numerically solve the dam break problem. The initial data are

$$\rho(x,0)=1+\tanh(x+4)-\tanh(x-4),\quad u(x,0)\equiv 0,$$

and the computational domain is $[-12\pi,12\pi]$.

In this case, no exact solution of the 2CH system is available and we therefore test the convergence of the FV and FVP methods towards the reference solution, which is obtained using the proposed FV method with 25000 mesh cells. In Fig. 1, we show the densities and velocities computed at the final time $t=2$ using $N_x=N_p=100$. As one can observe, both FV and FVP methods achieve high resolution though the results computed by the FVP method seem to be a bit sharper. We then perform a mesh refinement study and report the L^1-errors and experimental rates of convergence in Tables 1 and 2. As one can see, while both the FV and FVP methods achieve the expected second order of accuracy, the FVP errors are almost twice smaller than the FV ones.

Table 1: Example 1: L^1-errors in density.

$N_x=N_p$	$\|\rho^{\rm ref}-\rho^{\rm FV}\|_1$	Rate	$\|\rho^{\rm ref}-\rho^{\rm FVP}\|_1$	Rate
100	0.9521	–	0.6024	–
200	0.4067	1.23	0.2474	1.28
400	0.1348	1.59	0.0684	1.85
800	0.0365	1.89	0.0177	1.95
1600	0.0085	2.10	0.0037	2.25

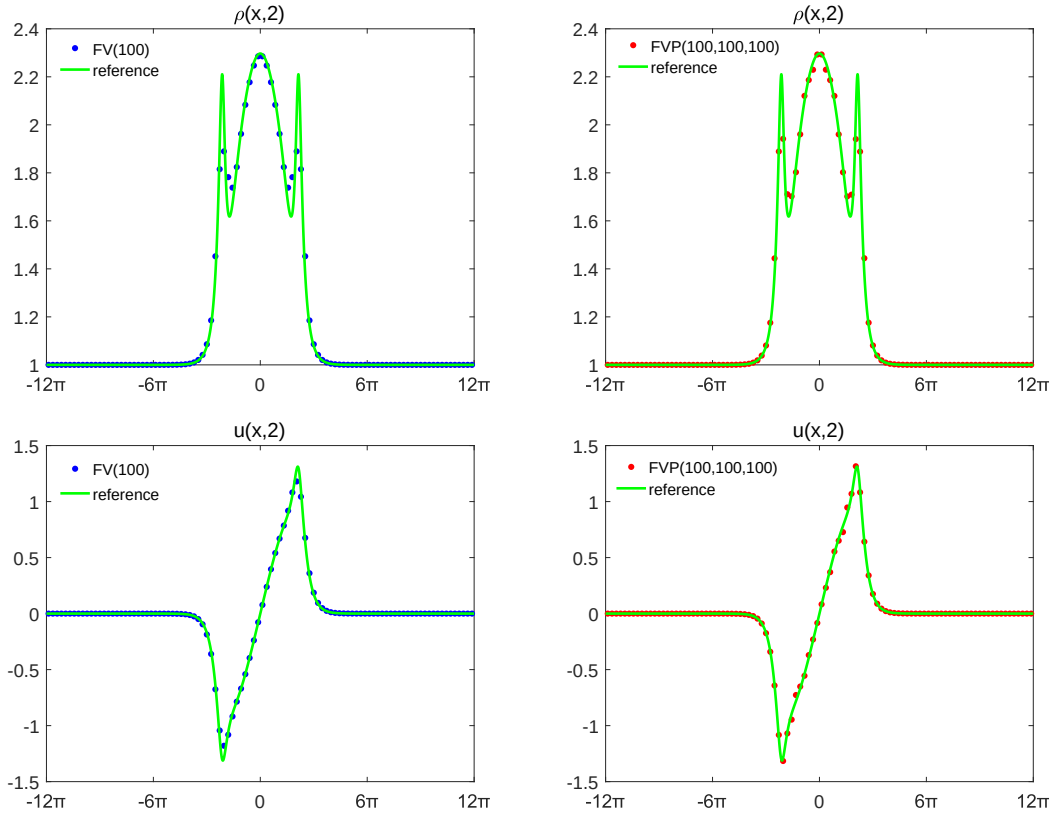

Figure 1: Example 1: Densities (top row) and velocities (bottom row) computed by the FV (left column) and FVP (right column) methods.

Table 2: Example 1: L^1-errors in velocity.

$N_x=N_p$	$\|u^{\text{ref}}-u^{\text{FV}}\|_1$	Rate	$\|u^{\text{ref}}-u^{\text{FVP}}\|_1$	Rate
100	0.4867	–	0.3729	–
200	0.2136	1.19	0.1036	1.85
400	0.0688	1.63	0.0261	1.96
800	0.0177	1.96	0.0060	2.17
1600	0.0044	2.02	0.0016	1.94

Example 2 — Single peakon

In the second example, we numerically solve a single peakon problem with the following initial conditions (see [23,46,57]):

$$\rho(x,0)\equiv 0.5,\quad u(x,0)=e^{-|x-10|},$$

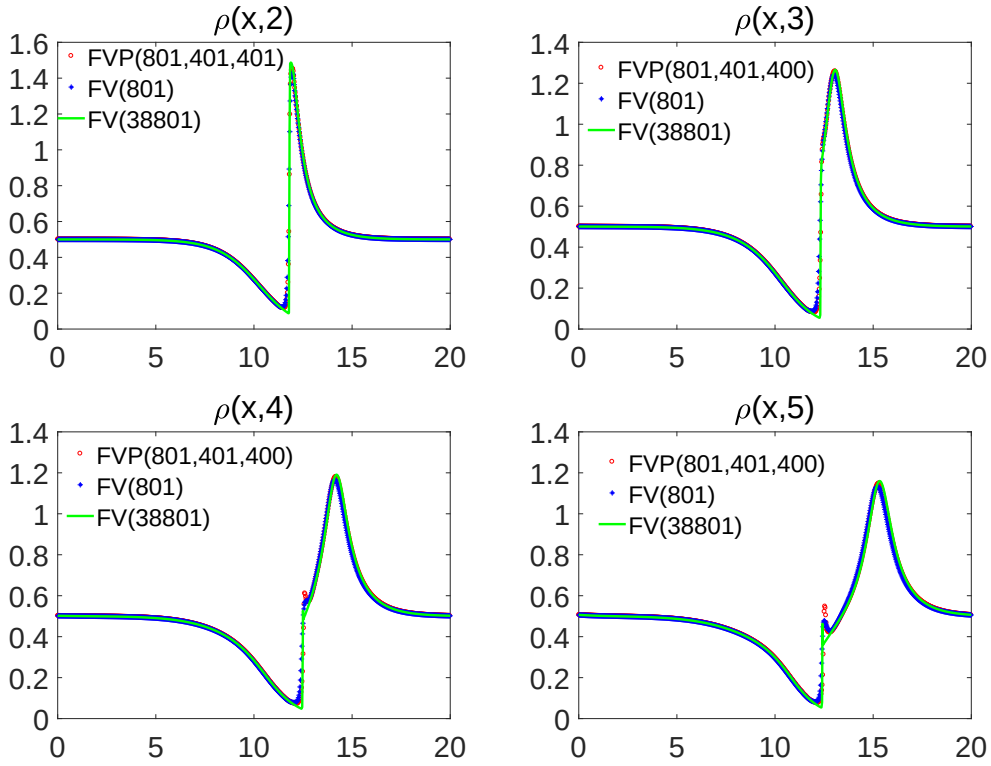

Figure 2: Example 2: Densities computed by the FV and FVP methods at four different times.

prescribed in the computational domain $[0,20]$. We use the FV method with $N_x=801$ and the FVP method with the same $N_x=801$, but twice smaller $N_p=401$. The solutions (ρ and u) computed at times $t=2$, 3, 4 and 5 are plotted in Figs. 2 and 3. Comparing the obtained results with those reported in [57] and the reference solution obtained by the FV method with $N_x=38801$, one can conclude that the FVP method produces slightly more accurate results even though the number of particles is relatively small.

In order to further study the performance of the FV and FVP methods, we notice that the exact solutions of the 2CH system preserve the Hamiltonians, which for $\alpha=1$ and $g=1$ are defined by

$$\mathcal{H}_1=\frac{1}{2}\int\limits_\Omega\left(u^2+u_x^2+\rho^2\right)\mathrm{d}x=\frac{1}{2}\int\limits_\Omega\left(mu+\rho^2\right)\mathrm{d}x,$$

and

$$\mathcal{H}_2=\frac{1}{2}\int\limits_\Omega\left(u^3+uu_x^2+u\rho^2\right)\mathrm{d}x=\frac{1}{2}\int\limits_\Omega\left(m(u^2-u_x^2)-u_x^2u_{xx}+u\rho^2\right)\mathrm{d}x;$$

see [46,57]. We now check how well the FV and FVP methods preserve the corresponding

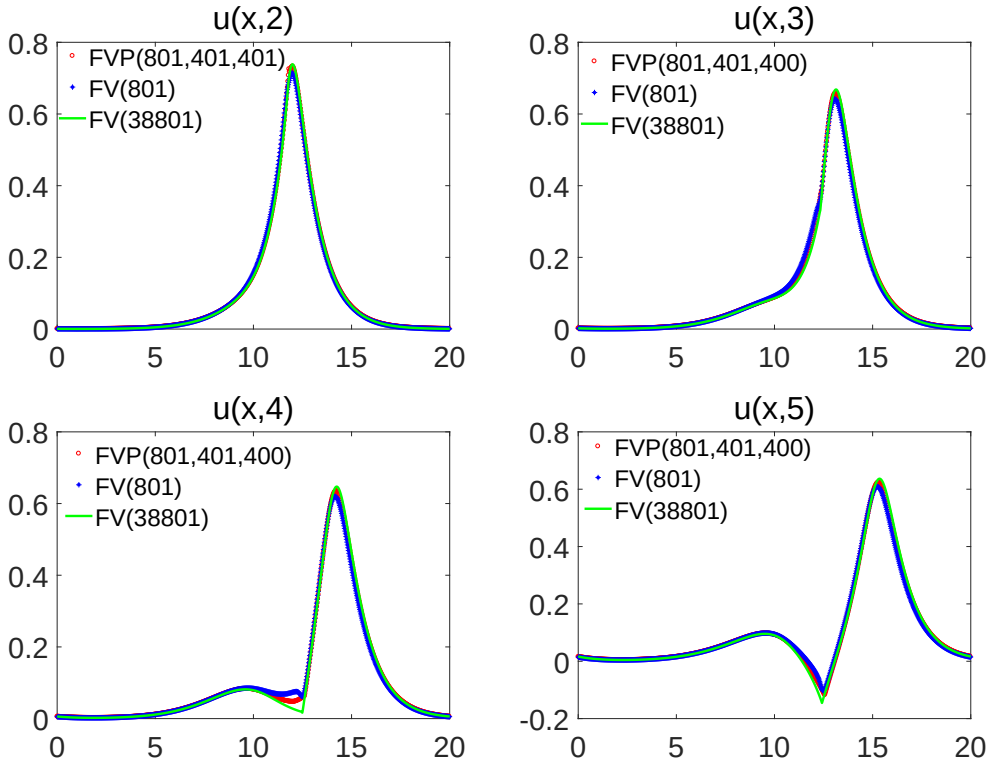

Figure 3: Example 3: Velocities computed by the FV and FVP methods at four different times.

discrete Hamiltonians. For the FV method, they are defined by

$$\mathcal{H}_1^{\rm FV}=\frac{\Delta x}{2}\sum_{j=1}^{N_x}\Big\{\overline{m}_j u_j+\overline{\rho}_j^2\Big\}\quad\text{and}\quad\mathcal{H}_2^{\rm FV}=\frac{\Delta x}{2}\sum_{j=1}^{N_x}\Big\{\overline{m}_j\big(u_j^2-(u_j)_x^2\big)-(u_j)_x^2(u_j)_{xx}+u_j\overline{\rho}_j^2\Big\},$$

where $\Delta x=20/N_x$ is the size of the FV cells and the quantities u_j, $(u_j)_x$ and $(u_j)_{xx}$ are computed as follows. We use the second-order finite-difference central scheme to solve the modified Helmholtz equation (1.1c) and recover the point values $\{u_j\}$ from the cell averages $\{\overline{m}_j\}$ and then calculate $(u_j)_x:=(u_{j+\frac{1}{2}}-u_{j-\frac{1}{2}})/\Delta x$ and $(u_j)_{xx}=(u_{j+1}-2u_j+u_{j-1})/\Delta x^2$. For the FVP method, both $\mathcal{H}_1$ and $\mathcal{H}_2$ have a well-defined reduction for all N-peakon solutions (2.12), (2.13) and (2.16). Moreover, by differencing (2.16) with $\alpha=1$, we obtain

$$u_{xx}^N(x,t)=\sum_{j=1}^{N}w_j(t)e^{-|x-x_j^{\rm p}(t)|}\left(\frac{1}{2}-\delta(x-x_j^{\rm p}(t))\right).$$

Therefore, the discrete Hamiltonians can be defined by

$$\mathcal{H}_1^{\rm FVP}=\frac{1}{4}\sum_{i,j=1}^{N_p}\Big\{w_iw_je^{-|x_i^{\rm p}-x_j^{\rm p}|}\Big\}+\frac{\Delta x}{2}\sum_{j=1}^{N_x}\overline{\rho}_j^2 \tag{3.1}$$

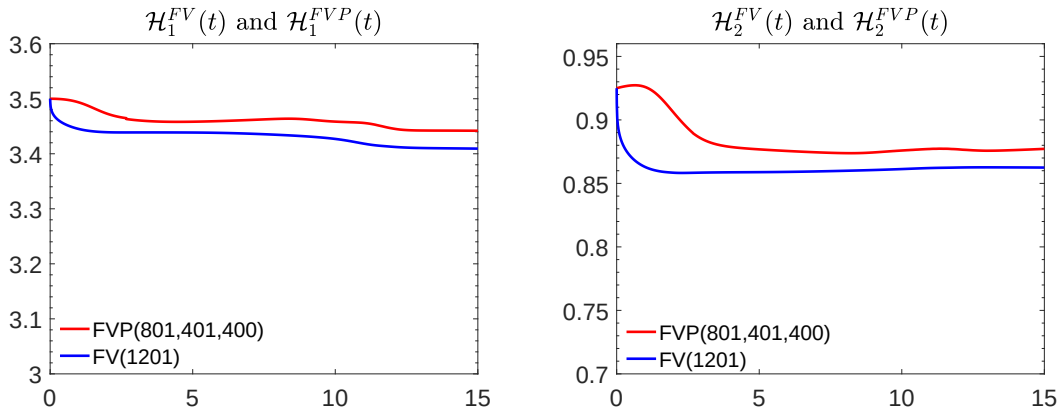

Figure 4: Example 2: The discrete Hamiltonians $\mathcal{H}_1^{\rm FV}$ and $\mathcal{H}_1^{\rm FVP}$ (left) and $\mathcal{H}_2^{\rm FV}$ and $\mathcal{H}_2^{\rm FVP}$ (right) as functions of t.

and

$$\mathcal{H}_2^{\rm FVP}=\frac{1}{8}\sum_{i=1}^{N_p}\sum_{j=1}^{N_p}\sum_{k=1}^{N_p}\Big\{w_iw_jw_ke^{-|x_i^{\rm p}-x_j^{\rm p}|-|x_i^{\rm p}-x_k^{\rm p}|}\Big\}+\frac{\Delta x}{2}\sum_{j=1}^{N_x}u^{N_p}(x_j,t)\overline{\rho}_j^2$$
$$-\frac{1}{24}\sum_{i=1}^{N_p}\Big\{\big((u_x)_i^{\rm p}\big)^2u_i^{\rm p}+\big((u_x)_{i+1}^{\rm p}\big)^2u_{i+1}^{\rm p}+4\big((u_x)_{i+\frac12}^{\rm p}\big)^2u_{i+\frac12}^{\rm p}\Big\}(x_{i+1}^{\rm p}-x_i^{\rm p}),\qquad(3.2)$$

where $u_i^{\rm p}:=u^{N_p}(x_i^{\rm p}(t),t)$, $u_{i+\frac12}^{\rm p}:=u^{N_p}(x_{i+\frac12}^{\rm p}(t),t)$, $(u_x)_i^{\rm p}:=u_x^{N_p}(x_i^{\rm p}(t),t)$ and $(u_x)_{i+\frac12}^{\rm p}:=u_x^{N_p}(x_{i+1/2}^{\rm p}(t),t)$ are computed using (2.13) and (2.16), respectively, and $x_{N_p+1}^{\rm p}(t)\equiv x_1^{\rm p}(t)$ by periodicity.

Since the FV method is less accurate, we use $N_x=1201$ for the FV method and $N_x=801, N_{\rm p}=401$ for the FVP method. The obtained results are presented in Fig. 4, where we plot the discrete Hamiltonians as functions of time. As one can see, the FVP method preserves the Hamiltonians much better than its FV counterpart. Moreover, for the FVP method, we can use less grid cells and particles to well preserve the discrete Hamiltonians.

Example 3 — Peakon anti-peakon interaction

In the third example, we numerically study the peakon anti-peakon interaction cases, which were considered previously in [23, 46, 57]. We take a zero total momentum initial data

$$\rho(x,0)\equiv0.5,\quad u(x,0)=e^{-|x+5|}-e^{-|x-5|},$$

and the computational domain is $[-20,20]$. We solve the underlying problem by both the FV and FVP methods using $N_x=804$ and $N_p=404$. We also compute a reference solution using the FV method on a finer mesh with $N_x=38804$. In Figs. 5 and 6, we

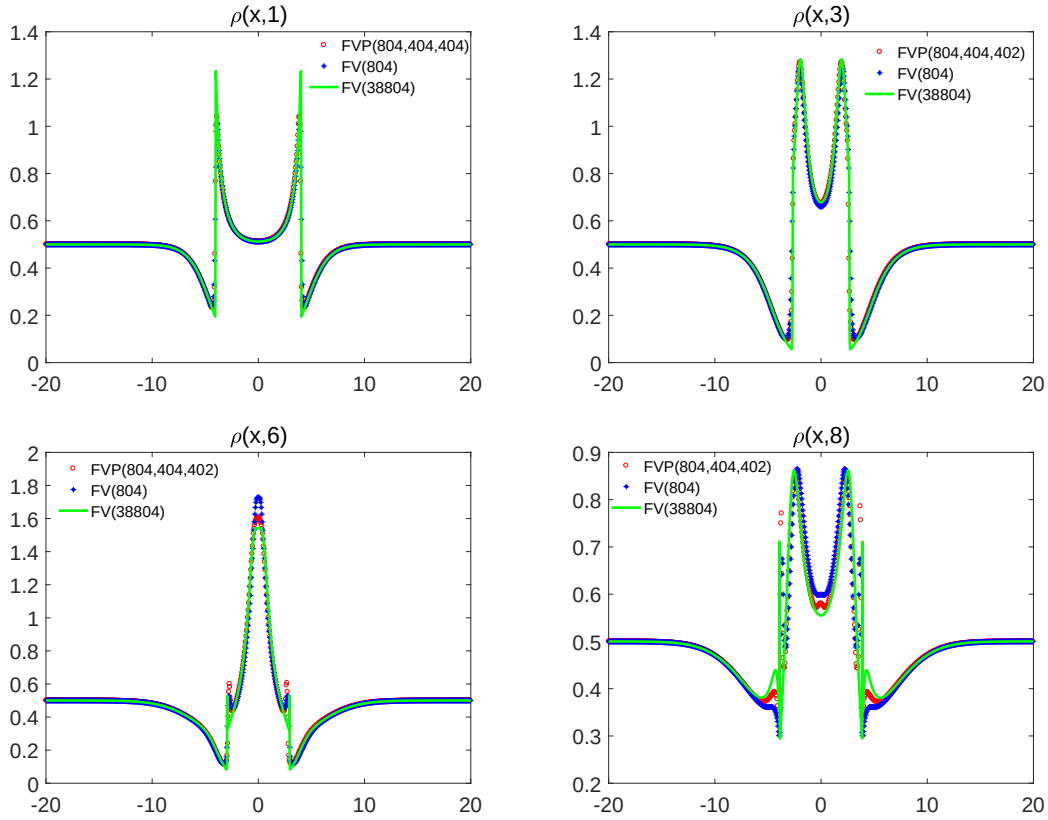

Figure 5: Example 3: Densities at different times computed by the FV and FVP methods.

plot the obtained solutions (ρ and u) at times $t=1$, 3, 6 and 8. We observe an elastic collision among the peakon solutions for a sufficiently large t, same as the numerical experiments in [46], the dynamics of the solutions are numerically caught well. Moreover, if we compare the solutions obtained by FV and FVP methods using the same FV cells, we can find that, the FVP method with less particles will achieve more accurate results.

3.2 Solitary wave propagation

In this section, we study the relationship between the studied 2CH and classical SV systems and compare the performance of each one of these systems in the context of solitary wave propagation. To this end, we first consider a motion of a shallow water over a flat bottom; see Fig. 7 and assume that the motion is in the x-direction and the physical variables do not depend on the second spatial variable y. In addition, we denote by H the mean level of water and by a and λ typical amplitude and wavelength of the wave, respectively. Our goal is to demonstrate that the studied 2CH system can serve as an asymptotic model of the classical shallow water equations and the physical validity of

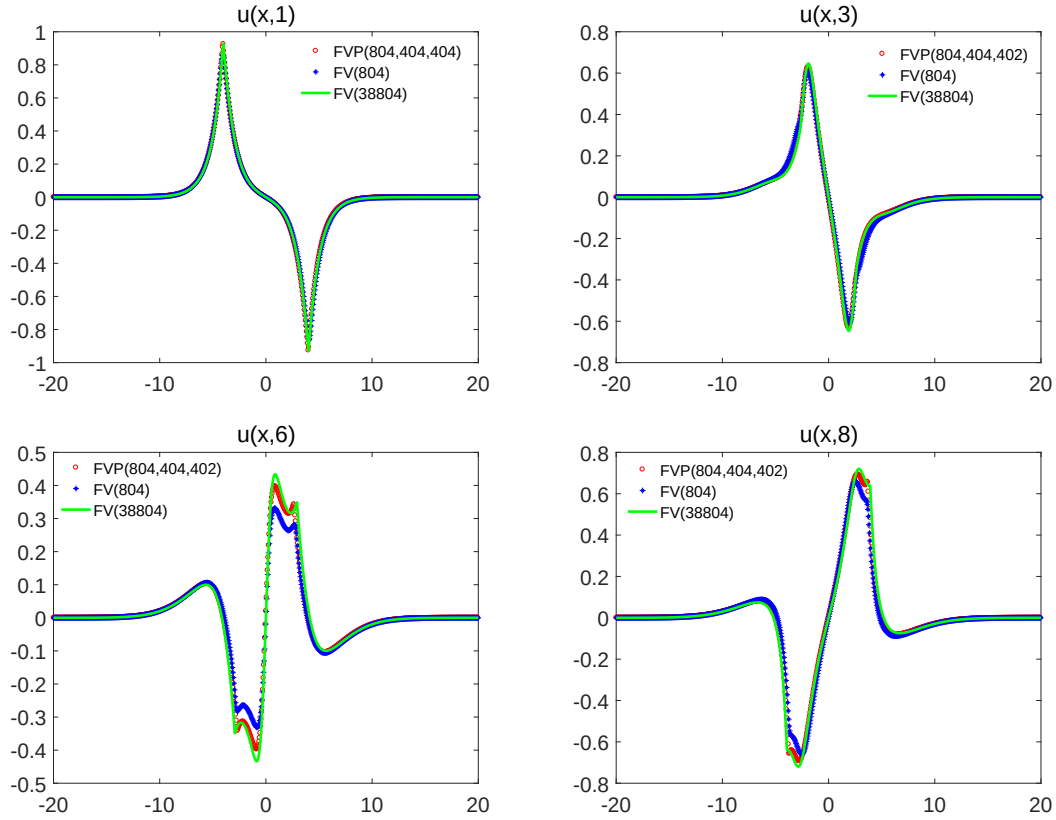

Figure 6: Example 3: Velocities at different times computed by the FV and FVP methods.

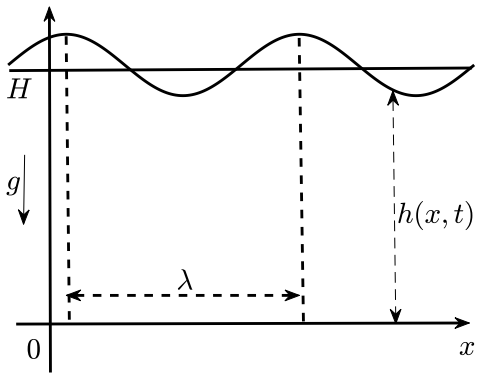

Figure 7: Water waves: general setting and notation.

the model depends on the characteristics of the flow under consideration. More precisely, this depends on particular assumptions made on the dimensionless parameters $\varepsilon = a/H$ and $\delta = H/\lambda$. The shallow water (or long wave) regime is characterized by the presump-

tion of small depth or long wavelength, and in order to incorporate stronger nonlinearity so that the model can capture observed interesting phenomena in nature such as waves of greatest height, the two parameters should satisfy the so-called CH scaling: $\delta \ll 1$ and $\varepsilon = \mathcal{O}(\delta)$.

We now consider the classical SV system of shallow water equations,

$$\begin{aligned} &h_t + (hv)_x = 0, \\ &(hv)_t + \Big(hv^2 + \frac{1}{2}gh^2\Big)_x = 0, \end{aligned} \tag{3.3}$$

and rewrite it the following nonconservative form:

$$\begin{aligned} &h_t + (hv)_x = 0, \\ &v_t + vv_x + gh_x = 0. \end{aligned} \tag{3.4}$$

which is equivalent to (3.3) for smooth solutions.

We then take into account the magnitude of the physical quantities (for details, see [25,32–34]), introduce the following dimensionless quantities:

$$x' = \frac{x}{\lambda}, \quad t' = \frac{\sqrt{gH}}{\lambda}t, \quad \varepsilon v' = \frac{v}{\sqrt{gH}}, \quad h' = \frac{h}{H},$$

and rewrite the system (3.4) in terms of the dimensionless variables x', t', h', v',

$$\begin{aligned} &h'_{t'} + \varepsilon (h'v')_{x'} = 0, \\ &\varepsilon v'_{t'} + \Big(h' + \frac{1}{2}\varepsilon^2 (v')^2\Big)_{x'} = 0. \end{aligned} \tag{3.5}$$

Next, we introduce $\eta := \frac{1}{\varepsilon}(h'-1)$, which describes the deviation of the water surface from the average level H. Substituting $h' = 1+\varepsilon\eta$ into (3.5) yields

$$\begin{aligned} &\eta_{t'} + \Big[(1+\varepsilon\eta)v'\Big]_{x'} = 0, \\ &v'_{t'} + \Big[\eta + \frac{1}{2}\varepsilon (v')^2\Big]_{x'} = 0. \end{aligned} \tag{3.6}$$

We note that if ε is sufficiently small, then (3.6) implies that $\eta_{t'} \approx -v'_{x'}$ and $v'_{t'} \approx -\eta_{x'}$.

On the other hand, let us define a new variable

$$\rho := 1 + \frac{1}{2}\varepsilon\eta - \frac{1}{8}\varepsilon^2 (v')^2 - \frac{1}{8}\varepsilon^2\eta^2, \tag{3.7}$$

for which one can easily obtain the following equalities:

$$\begin{aligned} \rho_{t'} &= \frac{1}{2}\varepsilon\eta_{t'} - \frac{1}{4}\varepsilon^2 v' v'_{t'} - \frac{1}{4}\varepsilon^2 \eta\eta_{t'} \\ &\approx \frac{1}{2}\varepsilon\eta_{t'} - \frac{1}{4}\varepsilon^2 v'(-\eta_{x'}) - \frac{1}{4}\varepsilon^2\eta(-v'_{x'}) = \frac{1}{2}\varepsilon\eta_{t'} + \frac{1}{4}\varepsilon^2 (\eta v')_{x'}, \end{aligned}$$

and

$$\begin{aligned}\frac{\varepsilon}{2}(\rho v')_{x'}&=\frac{\varepsilon}{2}\Big(v'+\frac{1}{2}\varepsilon\eta v'-\frac{1}{8}\varepsilon^2(v')^3-\frac{1}{8}\varepsilon^2\eta^2 v'\Big)_{x'}\\&=\frac{1}{2}\varepsilon v'_{x'}+\frac{1}{4}\varepsilon^2(\eta v')_{x'}-\frac{\varepsilon^3}{16}\Big((v')^3+\eta^2 v'\Big)_{x'}.\end{aligned}\tag{3.8}$$

Neglecting the ε^3 terms in (3.8), we obtain a conservation of mass type equation for ρ:

$$\rho_{t'}+\frac{\varepsilon}{2}(\rho v')_{x'}\approx\frac{\varepsilon}{2}\Big(\eta_{t'}+v'_{x'}+\varepsilon(\eta v')_{x'}\Big)=0.\tag{3.9}$$

Furthermore, using (3.7) results in

$$\rho^2=1+\varepsilon\eta+\frac{1}{4}\varepsilon^2\eta^2-\frac{1}{4}\varepsilon^2(v')^2-\frac{1}{4}\varepsilon^2\eta^2+\cdots\approx1+\varepsilon\eta-\frac{1}{4}\varepsilon^2(v')^2,$$

and then using the second equation in (3.5), we derive the following equation for the velocity v':

$$\varepsilon v'_{t'}+\Big(\frac{3}{4}\varepsilon^2(v')^2+\rho^2\Big)_{x'}\approx\varepsilon v'_{t'}+\Big(1+\varepsilon\eta+\frac{1}{2}\varepsilon^2(v')^2\Big)_{x'}=\varepsilon\Big\{v'_{t'}+\Big[\eta+\frac{1}{2}\varepsilon(v')^2\Big]_{x'}\Big\}=0.\tag{3.10}$$

Rescaling the independent variables one more time:

$$x''=\lambda x',\quad t''=\frac{\lambda}{\sqrt{gH}}t',\quad v''=\frac{1}{2}\sqrt{gH}\varepsilon v',\quad \rho''=\sqrt{H}\rho,$$

renaming $u:=v''$ and dropping the double prime notation for x'',t'' and ρ'', equations (3.9) and (3.10) are reduced to the dispersionless $(\alpha=0)$ version of the 2CH system (1.1), which can be written as

$$\begin{aligned}&\rho_t+(\rho u)_x=0,\\&u_t+\Big(\frac{3}{2}u^2+\frac{g}{2}\rho^2\Big)_x=0.\end{aligned}$$

Finally, based on the previous derivations, we can obtain the following relation between ρ, u, v and h in the dimensional units:

$$\rho=\sqrt{H}\Big(1+\frac{1}{2}\Big(\frac{h}{H}-1\Big)-\frac{1}{8}\Big(\frac{h}{H}-1\Big)^2-\frac{v^2}{8gH}\Big)\quad\text{and}\quad u=\frac{v}{2}.$$

Example 4

We now consider a numerical example (taken from [4]), in which we take $g=9.81$, $[0,200]$ computational domain and the following initial data that correspond to a solitary wave:

$$h(x,0)=1+\frac{1}{10}\operatorname{sech}^2\Big(\sqrt{\frac{3}{40}}(x-70)\Big),\quad v(x,0)=\frac{\sqrt{g}}{10}\operatorname{sech}^2\Big(\sqrt{\frac{3}{40}}(x-70)\Big).$$

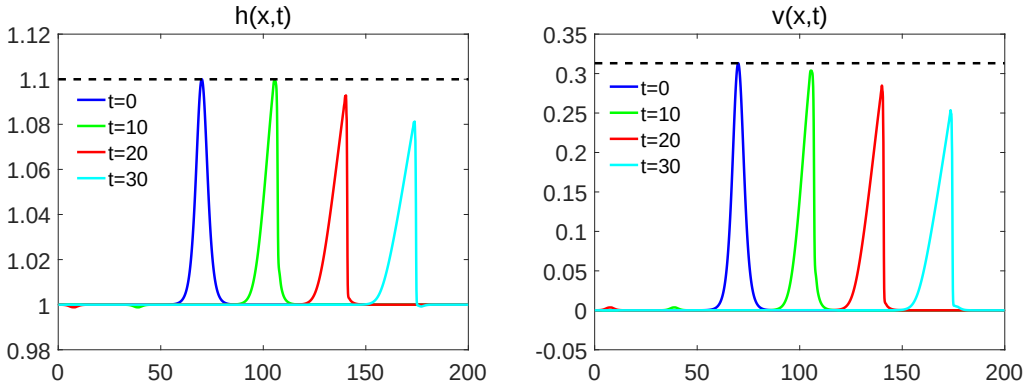

Figure 8: Example 4, $\alpha=0$: Time evolution of the water depth (left) and velocity (right).

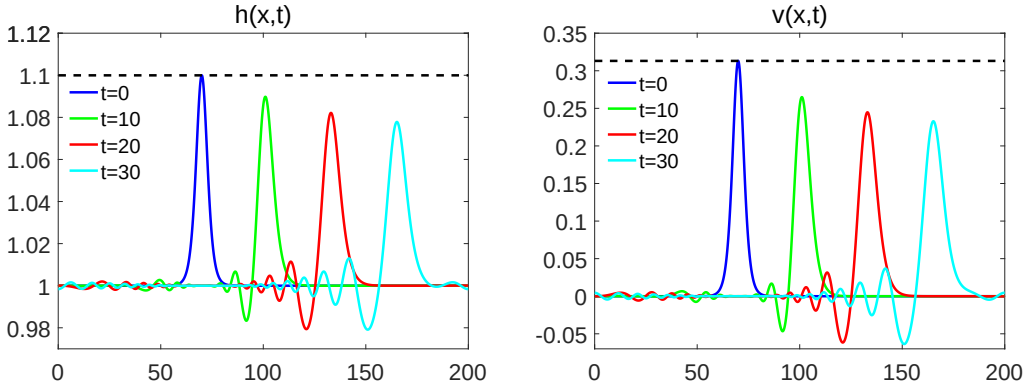

Figure 9: Example 4, $\alpha=1$: Time evolution of the water depth (left) and velocity (right).

In our numerical experiments below, we show how the speed and magnitude of the solitary wave is affected by the choice of α, which are taken to be $\alpha=0$, 0.6 and 1. At it was mentioned in [4], the classical Saint-Venant system fails to model the long time propagation of the solitary wave since its magnitude decreases and shape is destroyed over time. The same is true for the nondispersive ($\alpha=0$) 2CH system, as it can be clearly seen in Fig. 8, where we plot the numerical solution computed using the FV method with $N_x=1600$. Next, we consider the dispersive case by choosing $\alpha\neq 0$. One, however, must be careful not to introduce too much dispersion, as in this case the wave magnitude decays and solitary wave profile is getting destroyed. The latter can be illustrated by taking $\alpha=1$ and computing the solution of the 2CH system using the FVP method with $N_x=N_p=1600$. The time evolution of the computed solution is shown in Fig. 9, where one can observe both the wave dissipate and development of the growing tail of the wave train. We thus take a smaller dispersion by setting $\alpha=0.6$ and compute the numerical solution using exactly the same numerical setting (the FVP method with $N_x=N_p=1600$). The obtained results are presented in Fig. 10, where one can see that the shape of the

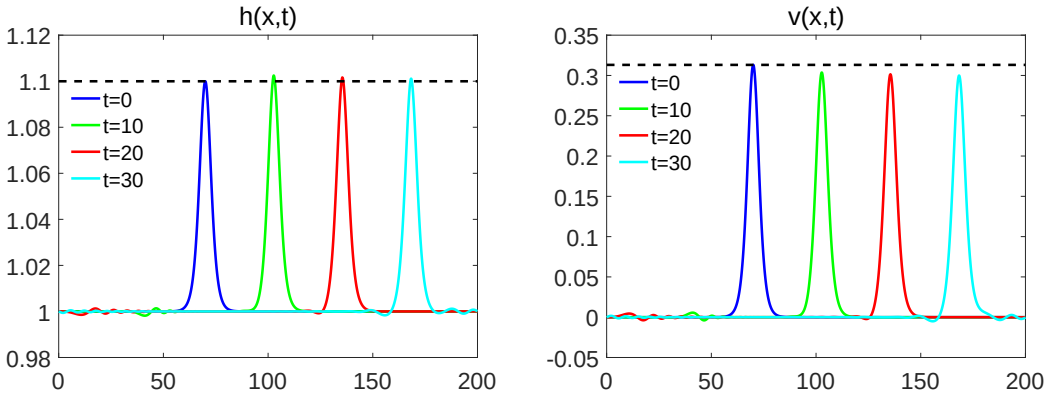

Figure 10: Example 4, $\alpha=0.6$: Time evolution of the water depth (left) and velocity (right).

traveling solitary wave is substantially better preserved while the dispersive wave train is much smaller than in the case of $\alpha=1$.

Our results suggest that the 2CH system (1.1) may be a good model for long time solitary wave propagation and that the hybrid FVP method may serve as a robust and accurate tool for studying the underlying system.

4 Conclusion

In this paper, we have introduced two numerical methods for solving the 2CH system (1.1), which was derived in the context of shallow water wave theory. From Example 4 in Section 3.2, one can conclude that for certain values of the dispersion parameter α the 2CH system represents a viable model for the long time propagation of tsunami-type waves. Using the developed numerical methods, we have illustrated that for these values of α, the amplitude and speed of the waves were preserved for longer times than those generated by the non-dispersive system, which is, in fact, equivalent to the classical Saint-Venant system. We have also been able to explicitly showcase some of the advantages that a hybrid FVP method holds over the FV central-upwind scheme. We would like to emphasize that in this paper, we have only provided an initial study of numerically solving (1.1) from the viewpoint of a model for the propagation of tsunami waves. Further studies will be conducted to better understand the effects of changing the length scale α on the solutions generated from solving the 2CH system.

Acknowledgments

The work of A. Chertock was supported in part by NSF grants DMS-1521051 and DMS-1818684. The work of A. Kurganov was supported in part by NSFC grant 11771201.

References

[1] E. Barthelemy, Nonlinear shallow water theories for coastal waves, Surveys in Geophysics, 25 (2004), 315–337.
[2] J. L. Bona, M. Chen, and J.-C. Saut, Boussinesq equations and other systems for small-amplitude long waves in nonlinear dispersive media. I. Derivation and linear theory, J. Nonlinear Sci., 12 (2002), 283–318.
[3] J. L. Bona, M. Chen, and J.-C. Saut, Boussinesq equations and other systems for small-amplitude long waves in nonlinear dispersive media. II. The nonlinear theory, Nonlinearity, 17 (2004), 925–952.
[4] M.-O. Bristeau, N. Goutal, and J. Sainte-Marie, Numerical simulations of a non-hydrostatic shallow water model, Comput. & Fluids, 47 (2011), 51–64.
[5] M.-O. Bristeau and J. Sainte-Marie, Derivation of a non-hydrostatic shallow water model; comparison with Saint-Venant and Boussinesq systems, Discrete Contin. Dyn. Syst. Ser. B, 10 (2008), 733–759.
[6] E. Bryant, Tsunami: the Underrated Hazard, Cambridge University Press, Oxford, England, second ed., 2008.
[7] R. Camassa and D. D. Holm, An integrable shallow water equation with peaked solitons, Phys. Rev. Lett., 71 (1993), 1661–1664.
[8] R. Camassa, J. Huang, and L. Lee, On a completely integrable numerical scheme for a nonlinear shallow-water wave equation, J. Nonlinear Math. Phys., 12 (2005), 146–162.
[9] R. Camassa, J. Huang, and L. Lee, Integral and integrable algorithms for a nonlinear shallow-water wave equation, Journal of Computational Physics, 216 (2006), 547–572.
[10] M. J. Castro Díaz, A. Kurganov, and T. Morales de Luna, Path-conservative central-upwind schemes for nonconservative hyperbolic systems. Preprint.
[11] A. Chertock, S. Cui, A. Kurganov, and T. Wu, Well-balanced positivity preserving central-upwind scheme for the shallow water system with friction terms, Int. J. Numer. Methods Fluids, 78 (2015), 355–383.
[12] A. Chertock, P. Du Toit, and J. E. Marsden, Integration of the EPDiff equation by particle methods, M2AN Math. Model. Numer. Anal., 46 (2012), 515–534.
[13] A. Chertock, E. Kashdan, and A. Kurganov, Propagation of diffusing pollutant by a hybrid eulerian-lagrangian method, in Hyperbolic problems: theory, numerics, applications (Lyon 2006), S. Benzoni-Gavage and D. Serre, eds., Springer, 2008, 371–380.
[14] A. Chertock and A. Kurganov, On a hybrid finite-volume particle method, M2AN Math. Model. Numer. Anal, 38 (2004), 1071–1091.
[15] A. Chertock and A. Kurganov, On a practical implementation of particle methods, Appl. Numer. Math., 56 (2006), 1418–1431.
[16] A. Chertock, A. Kurganov, J. Miller, and J. Yan, Central-upwind scheme for a non-hydrostatic Saint-Venant system. To appear in Proceedings of the XVII International Conference on Hyperbolic Problems: Theory, Numerics, Applications (University Park, 2018).
[17] A. Chertock, A. Kurganov, and G. Petrova, Finite-volume-particle methods for models of transport of pollutant in shallow water, J. Sci. Comput., 27 (2006), 189–199.
[18] A. Chertock, A. Kurganov, and Y. Rykov, A new sticky particle method for pressureless gas dynamics, SIAM Journal on Numerical Analysis, 45 (2007), 2408–2441.
[19] A. Chertock and D. Levy, Particle methods for dispersive equations, J. Comput. Phys., 171 (2001), 708–730.
[20] A. Chertock and D. Levy, A particle method for the KdV equation, J. Sci. Comput., 17 (2002),

491–499.
[21] A. Chertock, J.-G. Liu, and T. Pendleton, Convergence analysis of the particle method for the Camassa-Holm equation, in Proceedings of the 13th International Conference on "Hyperbolic Problems: Theory, Numerics and Applications", P. G. Ciarlet and T.-T. Li, eds., Contemporary Applied Mathematics, 2012, 356–373.
[22] A. Chertock, J.-G. Liu, and T. Pendleton, Elastic collisions among peakon solutions for the camassa-holm equation, Applied Numerical Mathematics, 93 (2015), 30–46.
[23] D. Cohen, T. Matsuo, and X. Raynaud, A multi-symplectic numerical integrator for the two-component Camassa–Holm equation, J. Nonlinear Math. Phys., 21 (2014), 442–453.
[24] A. Constantin and R. I. Ivanov, On an integrable two-component Camassa-Holm shallow water system, Phys. Lett. A, 372 (2008), 7129–7132.
[25] A. Constantin and R. S. Johnson, On the non-dimensionalisation, scaling and resulting interpretation of the classical governing equations for water waves, J. Nonlinear Math. Phys., 15 (2008), 58–73.
[26] G.-H. Cottet and P. D. Koumoutsakos, Vortex methods, Cambridge University Press, Cambridge, 2000.
[27] A. J. C. de Saint-Venant, Thèorie du mouvement non-permanent des eaux, avec application aux crues des rivière at à l'introduction des marèes dans leur lit., C.R. Acad. Sci. Paris, 73 (1871), 147–154.
[28] P. DEGOND AND F. J. MUSTIELES, *A deterministic approximation of diffusion equations using particles*, SIAM J. Sci. Stat. Comp., 11 (1990), pp. 293–310.
[29] S. GOTTLIEB, D. KETCHESON, AND C.-W. SHU, *Strong stability preserving Runge-Kutta and multistep time discretizations*, World Scientific Publishing Co. Pte. Ltd., Hackensack, NJ, 2011.
[30] S. Gottlieb, C.-W. Shu, and E. Tadmor, Strong stability-preserving high-order time discretization methods, SIAM Rev., 43 (2001), 89–112.
[31] A. E. Green and P. M. Naghdi, A derivation of equations for wave propagation in water at variable depth, J. Fluid Mech., 78 (1976), 237–246.
[32] R. Ivanov, Two-component integrable systems modelling shallow water waves: the constant vorticity case, Wave Motion, 46 (2009), 389–396.
[33] R. S. JOHNSON, *A Modern Introduction to the Mathematical Theory of Water Waves*, Cambridge University Press, Cambridge, 1997.
[34] ——, Camassa-holm, korteweg-de vries and related models for water waves, J. Fluid. Mech., 457 (2002), 63–82.
[35] ——, The classical problem of water waves: a reservoir of integrable and nearly-integrable equations, Journal of Nonlinear Mathematical Physics, 10 (2003), 72–92.
[36] D. J. Korteweg and G. de Vries, On the change of form of long waves advancing in a rectangular canal and on a new type of long stationary waves, Philos. Mag., 39 (1895), 422–443.
[37] A. Kurganov and D. Levy, Central-upwind schemes for the saint-venant system, M2AN Math. Model. Numer. Anal., 36 (2002), 397–425.
[38] A. Kurganov and C.-T. Lin, On the reduction of numerical dissipation in central-upwind schemes, Commun. Comput. Phys., 2 (2007), 141–163.
[39] A. Kurganov and J. Miller, Central-upwind scheme for Savage-Hutter type model of submarine landslides and generated tsunami waves, Comput. Methods Appl. Math., 14 (2014), 177–201.
[40] A. Kurganov, S. Noelle, and G. Petrova, Semidiscrete central-upwind schemes for hyperbolic conservation laws and hamilton-jacobi equations, SIAM J. Sci. Comput., 23 (2001), 707–740. electronic.

[41] A. Kurganov and G. Petrova, A second-order well-balanced positivity preserving central-upwind scheme for the saint-venant system, Commun. Math. Sci., 5 (2007), 133–160.
[42] A. Kurganov and E. Tadmor, New high resolution central schemes for nonlinear conservation laws and convection-diffusion equations, J. Comput. Phys., 160 (2000), 241–282.
[43] R. J. LeVeque, D. L. George, and M. J. Berger, Tsunami modelling with adaptively refined finite volume methods, Acta Numer., 20 (2011), 211–289.
[44] K.-A. Lie and S. Noelle, On the artificial compression method for second-order nonoscillatory central difference schemes for systems of conservation laws, SIAM J. Sci. Comput., 24 (2003), 1157–1174.
[45] P.-L. Lions and S. Mas-Gallic, Une méthode particulaire déterministe pour des équations diffusives non linéaires, C. R. Acad. Sci. Paris Sér. I Math., 332 (2001), 369–376.
[46] H.-L. Liu and T. Pendleton, On invariant–preserving finite difference schemes for the camassa–holm equation and the two–component camassa–holm system, Commun. Comput. Phys., 19 (2016), 1015–1041.
[47] H. Nessyahu and E. Tadmor, Nonoscillatory central differencing for hyperbolic conservation laws, J. Comput. Phys., 87 (1990), 408–463.
[48] M. Ortiz, E. Reyes-Gomez, and H. Velez-Munoz, A fast preliminary estimation model for transoceanic tsunami propagation, Geofisica International, 39 (2000), 207–220.
[49] E. Pelinovsky, T. Talipova, and C. Kurkin, A.and Kharif, Nonlinear mechanism of tsunami wave generation by atmospheric disturbances, Natural Hazard and Earth Sci., 1 (2001), 243–250.
[50] M. Rahman, Water Waves: Relating Modern Theory to Advanced Engineering Practice., Clarendon Press, Oxford, England, second ed., 1995.
[51] P.-A. Raviart, An analysis of particle methods, in Numerical methods in fluid dynamics (Como, 1983), vol. 1127 of Lecture Notes in Math., Springer, Berlin, 1985, 243–324.
[52] A. B. Shabat and L. Martínez Alonso, On the prolongation of a hierarchy of hydrodynamic chains, in New trends in integrability and partial solvability, vol. 132 of NATO Sci. Ser. II Math. Phys. Chem., Kluwer Acad. Publ., Dordrecht, 2004, 263–280.
[53] C. Sulem and P.-L. Sulem, The nonlinear Schrödinger equation, vol. 139 of Applied Mathematical Sciences, Springer-Verlag, New York, 1999. Self-focusing and wave collapse.
[54] P. K. Sweby, High resolution schemes using flux limiters for hyperbolic conservation laws, SIAM J. Numer. Anal., 21 (1984), 995–1011.
[55] B. van Leer, Towards the ultimate conservative difference scheme. V. A second-order sequel to Godunov's method, J. Comput. Phys., 32 (1979), 101–136.
[56] G. B. Whitham, Linear and nonlinear waves, Wiley-Interscience [John Wiley & Sons], New York, 1974. Pure and Applied Mathematics.
[57] C.-H. Yu, B.-F. Feng, and T. W. H. Sheu, Numerical solution to a two-component camassa-holm equation, J. Comput. Appl. Math., 336 (2018), 317–337.